i

Inertial Navigation using Atom Interferometry

Jimmy Stammers
Imperial College London

A dissertation submitted for …

8331 (errors:1)

Abstract

This thesis describes work I did during my PhD...

Declaration

This dissertation is the result of my own work...

Jimmy Stammers

Acknowledgements

Some people worth thanking...

Preface

This thesis describes my research on various aspects of…

x

Contents

List of figures

List of tables

Chapter 1.

Introduction

- atom interferometry experiments for precision measurements of inertial forces

- inertial navigation suffers from long-term bias drift

- recent experiments have demonstrated measuring acceleration in environments of interest to navigation

Chapter 2.

Theory

- Describe general principles of light-matter interaction

- Specific cases for laser cooling (doppler/sub-doppler) and Raman transitions

- Lead into atom interferometry

- Perhaps split this into two shorter chapters

2.1. Overview

2.2. Light-Matter Interactions

2.3. Laser Cooling of Rubidium-87

2.4. Raman Transitions in Rubidium-87

2.5. Light Pulse Atom Interferometry

Chapter 3.

MOTMaster

3.1. Chapter Overview

The aim of this chapter is to provide a description of the MOTMaster software, which was developed from a pre-existing version during my PhD. The design of MOTMaster assumes very little about the particular experiment it is being used for, so much of the discussion in this chapter will be kept general. This chapter begins by motivating the need to extend MOTMaster by developing a graphical interface to simplify the creation of experimental sequences, as well as implementing new methods of controlling hardware. This is followed by a general description of how MOTMaster configures the various types of inputs and outputs used in an experiment.

3.2. Motivation

In the initial stages of my PhD, I decided to use Cicero Word Generator [1] to control the hardware for the experiment. This is a graphical-based control system developed by

Wolfgang Ketterle's group at MIT, which was designed for controlling atomic physics experiments using National Instruments hardware. Over time, as the experiment became more complex, it started to become apparent that Cicero was not suited to meet all of our requirements for control software. This was most evident in the control of the M-Squared Raman laser system. Unlike the Muquans laser system, which can be controlled externally using analogue and digital voltages and serial messages, the M-Squared system is externally controlled by communicating JSON messages to a web server. Implementing such a drastically different scheme for controlling a specific component into Cicero was not deemed worthwhile. Around this time, I also realised that Cicero takes an appreciable amount of time (around 300 ms) to re-calculate the experiment sequence between each shot. Since the design of Cicero was aimed at controlling experiments that take many seconds per cycle, this dead time between each cycle is not significant on those time scales. In contrast, each cycle of this experiment takes around 250 ms. This unnecessary dead time needed to be addressed if we hoped to improve the repetition rate.

After it became clear that a potentially large amount of work would be needed to improve Cicero, I decided that it was worth moving to a new control system. A collection of programs, named EDMSuite, has been developed by people in Centre for Cold Matter (CCM) to control a range of experiments within the group. One application, MOTMaster, was designed to control and acquire data from experiments investigating cold atoms trapped in a Magneto-optical Trap (MOT), as its name suggests. For this reason, it seemed the most appropriate software for our purposes. However, its method of structuring experimental sequences was inconvenient, as it lacked a graphical user interface to do so. During the process of switching to using MOTMaster to control the experiment, I designed a graphical method of structuring sequences, which functioned identically on a device level to the original method of defining sequences. In addition to this, I included an interface to the M Squared laser system,

so that it could be controlled using MOTMaster. As with other hardware interfaces, the M Squared interface is loosely coupled to the rest of MOTMaster, so that other experiments which do not use this laser can still use MOTMaster.

3.3. Interfacing wth Hardware

The majority of the experimental hardware is controlled using analogue and digital voltages that are generated by Data Acquisition (DAQ) cards manufactured by National Instruments. MOTMaster is compatible with cards that use either the NI-DAQmx or NI-HSDIO device drivers. These are used to configure the generation or acquisition of digital or analogue voltage waveforms and are capable of precisely timing and synchronising their I/O across multiple devices. Most components in the experiment rely on this precise timing to function correctly. Other devices, where timing accuracy is less critical, are controlled by sending or receiving data using serial communication. This has the advantage of allowing more structured command beyond analogue or digital voltages, but the communication speed of the serial channel limits the accuracy of the execution time. An understanding of the low-level interface between control software and the experiment is very useful in both carrying out experiments and accurately interpreting the results.

3.3.1. Hardware Abstraction

When designing software, it is often useful to structure a program in such a way that modules which make use of other components do not need to know about their specific implementation in order to use them. This approach, known as loose coupling, means that the submodule can be modified without harming the compatibility of these two components. In the context of experimental hardware, this is equivalent

to requiring that changing specific components, for example the Voltage-Controlled Oscillator (VCO) that generates the RF power for an Acousto-optic Modulator (AOM), will not stop the experiment from working. This is done using abstract representations of the hardware, in the form of input and output channels that are used to communicate to each device.

3.3.2. Voltage Pattern Generation

All the analogue outputs controlled using MOTMaster are done using the NI-DAQmx software. Each output uses a Digital-to-Analogue Converter (DAC) to convert a floating-point number into an analogue voltage. To generate a sequence of voltages across multiple channels, the NI-DAQmx driver allocates a block of memory on the DAQ card for each output channel. This memory acts as a first-in first-out (FIFO) buffer for data streamed to it from a computer. The output of each channel is synchronised to a clock signal, so that every time a rising edge occurs on the clock, the voltage at each output transitions to the value corresponding to the next value in its corresponding buffer. Channels across multiple DAQ cards can be synchronised by sharing a clock signal, which can be done using the bus that connects cards in a PXI-e chassis. Additional cards can also be configured to trigger the start of their output at the moment they receive the first clock pulse, rather than waiting for a software trigger from the computer.

Digital outputs from NI-DAQmx cards are generated in much the same way as analogue voltages, except for the fact that they only take two values corresponding to either a low (0 V) or high (3.3/5 V) level. DAQ cards which operate using the NI-HSDIO driver function differently. These cards have faster on-board clocks than is usually available with NI-DAQmx hardware. For instance, NI-DAQmx PXI-6723 can operate with a maximum clock frequency of 200 kHz and typical sequence durations
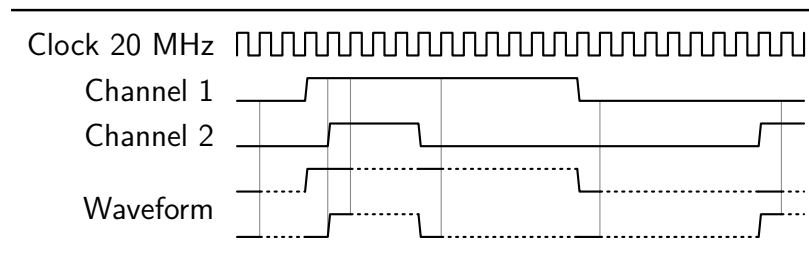
Figure 3.1.: Scripted pattern generation for an NI-HSDIO digital output card. A pattern is split into segments which correspond to a duration for which all the channels output a constant value. Each of these smaller waveforms are written to the on-board memory, along with a script that instructs the card to output each pattern for the required number of times to reconstruct the original sequence. By reducing the amount of memory required to define the sequence, a faster clock frequency and hence timing resolution can be used to output digital control signals.

mean that a sample rate of 100 kHz is needed to fit the entire sequence into memory. However, the NI-HSDIO PXI-6541 card can generate digital voltages at sample rates up to 50 MHz and requires less memory to store a pattern. Rather than write the pattern as an array of values for each sample, the sequence is segmented into smaller patterns during which the state of each channel is constant, as illustrated in Figure 3.1. NI-HSDIO cards can be scripted to generate each of these patterns for the appropriate number of clock cycles.

3.3.3. Timed Serial Communication

Serial communication is used to control devices which require more complex control than is possible using analogue or digital voltages. This increase in complexity comes at the cost of slower response times, because it takes longer to communicate an array of bytes is longer than to change the voltage across an output terminal. Using the NI-VISA driver, the output of serial data can only be timed using a software clock on a computer, which is more prone to jitter than a hardware clock. One way to improve the synchronisation between serial data and hardware timed outputs is to use extra hardware to trigger the transmission of serial data. If the trigger is timed using the
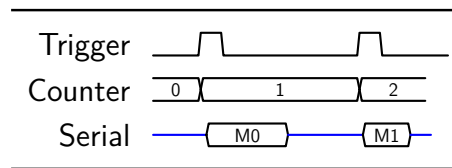
Figure 3.2.: Timing diagram for serial communication. A counter channel is configured to count edges from a digital output channel. Every time it sees a rising edge, it triggers the output of the next message on each serial channel from the computer. Multiple messages can be communicated during a single sequence without the need for software timing.

same clock as other outputs and the transmission delay is accounted for, then serial data can be output more synchronously. The scheme for timing serial messages is shown in Figure 3.2. Serial messages are stored as strings on the computer and a counter channel is configured so that every time it detects a rising edge, the computer outputs the next message. This counter is connected to a digital output channel, so that it acts as a trigger for the serial data output. Using this method, multiple serial messages can be sent to one device during a sequence even for devices which have no means of storing commands.

3.3.4. Voltage Acquisition

Analogue input channels are configured in a similar way to analogue output channels. A block of memory is allocated on the DAQ card for each input channel. Once the card is triggered to start acquiring, an Analogue-to-Digital Converter (ADC) converts the voltage across the input into a digital value at every rising edge of the clock signal. Once the sequence has finished, or the buffer has been filled, the card streams this data to the computer.

3.4. External Control

3.5. MOTMaster Sequences

In addition to interfacing with control hardware, MOTMaster is used to define the structure of experimental sequences. In earlier versions of MOTMaster, sequences were defined using functions within a C# source file. To run an experiment, MOTMaster compiled this file to build the voltage patterns and wrote them to the hardware. Whilst this had little overhead in resources needed to build and run a sequence, modifying and debugging sequences was much more time consuming. Taking inspiration from Cicero, the user interace of MOTMaster was redesigned so that sequences could be expressed graphically. They are then built using the same functions as before, so that from the point of view of the hardware, the two methods of control are equivalent.

3.5.1. Sequence Structure

A MOTMaster sequence is composed of a list of sequence steps, which define the state of the control hardware over a discrete amount of time. Each step is defined to last for a duration which must be an integer multiple of the timebase (e.g. $10\,\mu s$ for a $100\,kHz$ sample clock frequency). During a step, a digital channel is either high or low and each serial channel can send one message, which is encoded as a string of text. Analogue output channels can be configured to output a single voltage, step from one value to another, or linearly ramp to a specified value. A sequence step is useful to represent a single action, so that each stage of the experiment, for example the initial MOT loading phase, is composed of multiple steps. Numerical values, such as analogue voltages or times, can be represented by named parameters. The value of a parameter can be updated between each cycle of the experiment, so that MOTMaster can implement

a scan by iterating a parameter through a range of values. Besides determining the state of the output hardware, the sequence steps are used to define when to acquire from the analogue inputs. A specific digital channel, named `acquisitionTrigger`, is reserved as a start trigger for the acquisition. Analogue data starts being acquired during the step this channel goes high and stops when it goes low. Therefore, the number of samples required depends on the time between the first and last step and the analogue input sample clock frequency.

3.5.2. Running a Sequence

MOTMaster is designed to run in two modes, referred to as repeat and scan. The distinction between these is that the repeat mode does not need to recreate a sequence between each cycle. Before MOTMaster starts controlling the experiment, the sequence is built and the output hardware is configured to regenerate their patterns. In practice, this reduces the delay between each cycle, which is largely a result of the time needed to process acquired data and reconfigure the control hardware. In contrast, scan mode varies a parameter during each cycle, so additional time is required to rebuild the sequence and write to each DAQ card. Aside from this, these modes operate equivalently. At the start of an experiment cycle, the hardware is initialised and timing properties, such as the trigger and sample clock for each DAQ card is set. The sequence represented in the user interface is converted into the analogue and digital voltage patterns for each DAQ card. As mentioned previously, the required buffer for the analogue input data is calculated based on the state of the `acquisitionTrigger` channel. If any serial commands are used, the timing properties of the counter channel are configured, similarly to the rest of the **DAQ! (DAQ!)** hardware. The sequence is started by sending a software trigger to one output card, which is configured to export its start trigger to the other cards. This ensures that start of the output of each card is

synchronised. After the sequence has finished, any acquired data from the analogue input channels is streamed to the computer. The data per channel are segmented into arrays that were acquired during each sequence step, before additional post-processing if required. Finally, the hardware is reset to its initial state, before starting the next experiment cycle.

3.6. Experiment Control Hardware

In the preceding sections, the discussion of MOTMaster has been presented without referring to specific hardware used in this experiment. Subsequent chapters will introduce components of the experiment that are controlled by a computer, but it is worth introducing the hardware used to implement this control. All of the DAQ cards are housed on a PXIe 1073 chassis, so that timing signals such as start triggers and sample clocks can be shared on the PXI backplane in order to minimise the number of external cables required to synchronise the devices. The analogue output signals are generated on a PXI-6723 card. This contains 32 analogue output channels and the output of each is generated using a 13 bit DAC. Over the maximum voltage range of $\pm 10\,\text{V}$, this corresponds to an output quantisation of $2.44\,\text{mV}$, which did not limit the precision of any analogue control in the experiment. The analogue output pattern is sampled at a frequency of $100\,\text{kHz}$, which gives a minimum resolution of $10\,\mu\text{s}$. Any jitter on this sample clock did not produce any noticeable effects during the experiment. This card also contains the counter channel used to trigger serial messages.

Two cards on the chassis are able to acquire data from analogue inputs. The first is a PXIe-6341, which has 16 input channels, each with a 16-bit ADC. During the preliminary stages of the experiment, this bit-depth was sufficiently large to prevent quantisation effects becoming a dominant source of error. However, as discussed

further in Section 7.2.4, the AI Q 2010 MEMS accelerometer used in the experiment has a noise spectral density which necessitates a greater bit-depth ADC. Therefore, a PXI-4462 card, which contains 4 24-bit analogue input channels, was added. This card is used to acquire data from devices where the higher voltage resolution is desirable — namely, the MEMS accelerometer and detection photodiode.

Digital output signals are generated using a PXI-6541 card. Unlike the others, this card is controlled using the NI-HSDIO driver. With a maximum sampling frequency of 50 MHz, this card is capable of generating digital signals at a much higher rate than the PXIe-6341, which also contains digital output channels. However, the PXIe-6341 card only contains 8 digital channels that can be timed using a hardware clock, fewer than required to control the entire experiment. A second, historical, reason to use a card with greater timing resolution was to reduce the effects of timing inaccuracies on the interferometer phase. As discussed in Section **??**, a difference in the time between each interferometer pulse results in a phase difference which is independent of inertial forces and reduces sensitivity. Before the M Squared laser system was developed, the original plan was to use the μQuans laser to provide light for the interferometer and control the laser pulses using Transistor-transistor Logic Circuit (TTL) switches to an AOM and a shutter. In this case, the greater timing accuracy of the PXI-6541 was desirable. Since the M Squared laser contains a dedicated module to synthesise analogue and digital waveforms to control the interferometer pulses, this requirement on the timing accuracy of the digital channels controlled using MOTMaster is no longer necessary.

Two components of the experiment are controlled during the experiment using serial communication. The first of these is an interface to the Direct Digital Synthesiser (DDS) on the μQuans laser which control the frequency of the cooling and repump lasers and is controlled in real-time during the experiment. This communication protocol

is described in further detail in Section 5.3.1. In addition to this, a serial interface is used to control the frequency of a WindFreak microwave synthesiser. Its use in the experiment is described in Section 6.3.3. Unlike the μQuans laser, no serial data is sent to the WindFreak after the sequence starts. The output frequency is set between cycles and remains constant throughout. Finally, MOTMaster is configured to remotely connect to the M Squared laser, so that it can control all the parameters necessary to drive Raman transitions during the experiment. This is done by sending structured JSON messages that contain commands to implement this control. More detail on how this is used in the experiment is given in Section **??**.

Chapter 4.

Laser Systems

This chapter provides a description of the hardware that makes up the experiment. Over the course of the project, the complexity of the experiment necessarily increased. The setup is presented in a bottom-up approach, starting from the most fundamental components, to provide a clear overview of the system.

To-Do:

- Figures describing each of the lasers

- Describe 3D and 2D MOT setups

- Imaging systems

- Microwave synthesisers

- Raman Assembly

- MOT light distribution

4.1. Chapter Overview

The first two sections describe the two commercial laser systems used in this experiment. The μQuans laser system which generates the light used for cooling and repump in the 2D and 3D Magneto-optical Traps (MOTs), referred to as the MOT light. The design and operation of this laser is given in Section A.2. A secondary laser system, built by MSquared, is used to generate light to drive Raman transitions between two hyperfine ground states in Rubidium-87 (^{87}Rb)[1], otherwise referred to as Raman light. This is described in Section A.3.This is followed by a description of the vacuum chamber in Section **??** which contains both the 2D MOT (Section **??**) and the 3D MOT (Section **??**).

4.2. The μQuans Laser System

To-Do:

- Laser Schematic

- Plots of lock signals

- DDS Serial communication

- Power output, stability

- Ref for error signal generation by current modulation

- Move some of this to appendix

All the MOT light in this experiment was generated by the μQuans laser [2]. μQuans is a French laser company that is a spin-off from the Institut d'Optique and Observatoire

---

[1]The μQuans laser also has a pair of lasers designed for driving Raman transitions, but these are not used in this experiment. Section A.3 gives an explanation for this.

de Paris. Consequently, their technology has been developed over a long history of performing experiments into atom interferometry using Rubidium. A schematic of this laser system is shown in Figure A.1. The μQuans laser is comprised of four 1560nm **ecdls!**s (**ecdls!**s) which are frequency-doubled to produce light at wavelengths close to 780nm. The telecommunications industry, which relies heavily on light in the 1530-1565nm wavelength band for optical communications, has motivated a rapid development in low-noise, robust lasers. In particular, this has enabled a design which does not require free-space optics and is much more resilient to effects such as temperature changes and vibrations, when compared to more conventional 780nm laser systems. The μQuans laser contains one master laser [2], which is locked to the $F = 3 \rightarrow F' = 3, 4$ crossover point in Rubidium-85 (^{85}Rb), and serves as an absolute frequency reference. The other three slave lasers are used for output. The first one is used to provide lightAll the MOT light in this experiment was generated by the μQuans laser [2]. μQuans is a French laser company that is a spin-off from the Institut d'Optique and Observatoire de Paris. Consequently, their technology has been developed over a long history of performing experiments into atom interferometry using Rubidium. A schematic of this laser system is shown in Figure A.1. The μQuans laser is comprised of four 1560nm **ECDLs!**s (**ECDLs!**s) which are frequency-doubled to produce light at wavelengths close to 780nm. The telecommunications industry, which relies heavily on light in the 1530-1565nm wavelength band for optical communications, has motivated a rapid development in low-noise, robust lasers. In particular, this has enabled a design which does not require free-space optics and is much more resilient to effects such as temperature changes and vibrations, when compared to more conventional 780nm laser systems. The μQuans laser contains one master laser [3], which is locked to the $F = 3 \rightarrow F' = 3, 4$ crossover point in ^{85}Rb, and serves as an absolute frequency reference. The other three slave lasers are used for

---

[2] see Section A.2.1 for more details
[3] see Section A.2.1 for more details

output. The first one is used to provide light for cooling, as well as repump light by modulating the phase of this laser using an Electro-optic Modulator (EOM). The other two make up a pair of lasers for driving Raman transitions. One laser is frequency-offset locked to the master and the other is phase-locked to the first, to ensure that the relative phase between the two lasers is constant. It should be noted that this Raman laser was not used in this experiment, so will not be discussed in great detail. Each of these slave lasers is amplified in an Erbium-Doped Fibre Amplifier (EDFA) before being frequency doubled in a Periodically Poled Lithium Niobate (PPLN) and passed through an AOM which is used to control the output power during the experiment. for cooling, as well as repump light by modulating the phase of this laser using an EOM. The other two make up a pair of lasers for driving Raman transitions. One laser is frequency-offset locked to the master and the other is phase-locked to the first, to ensure that the relative phase between the two lasers is constant. It should be noted that this Raman laser was not used in this experiment, so will not be discussed in great detail. Each of these slave lasers is amplified in an EDFA before being frequency doubled in a PPLN and passed through an AOM which is used to control the output power during the experiment.

4.2.1. Absolute Frequency Reference

The purpose of the master laser is to provide an absolute frequency reference so that the frequency of the output lasers can be controlled by comparing the difference frequency between them and the master. Lasers with linewidths narrower than their natural linewidth can be achieved by using a servo to stabilise their frequency and is essential for any experiment that requires laser light of a precise frequency. The frequency reference for the master is obtained using saturated absorption spectroscopy inside a Rubidium vapor cell. The sub-Doppler features in this spectrum are insensitive
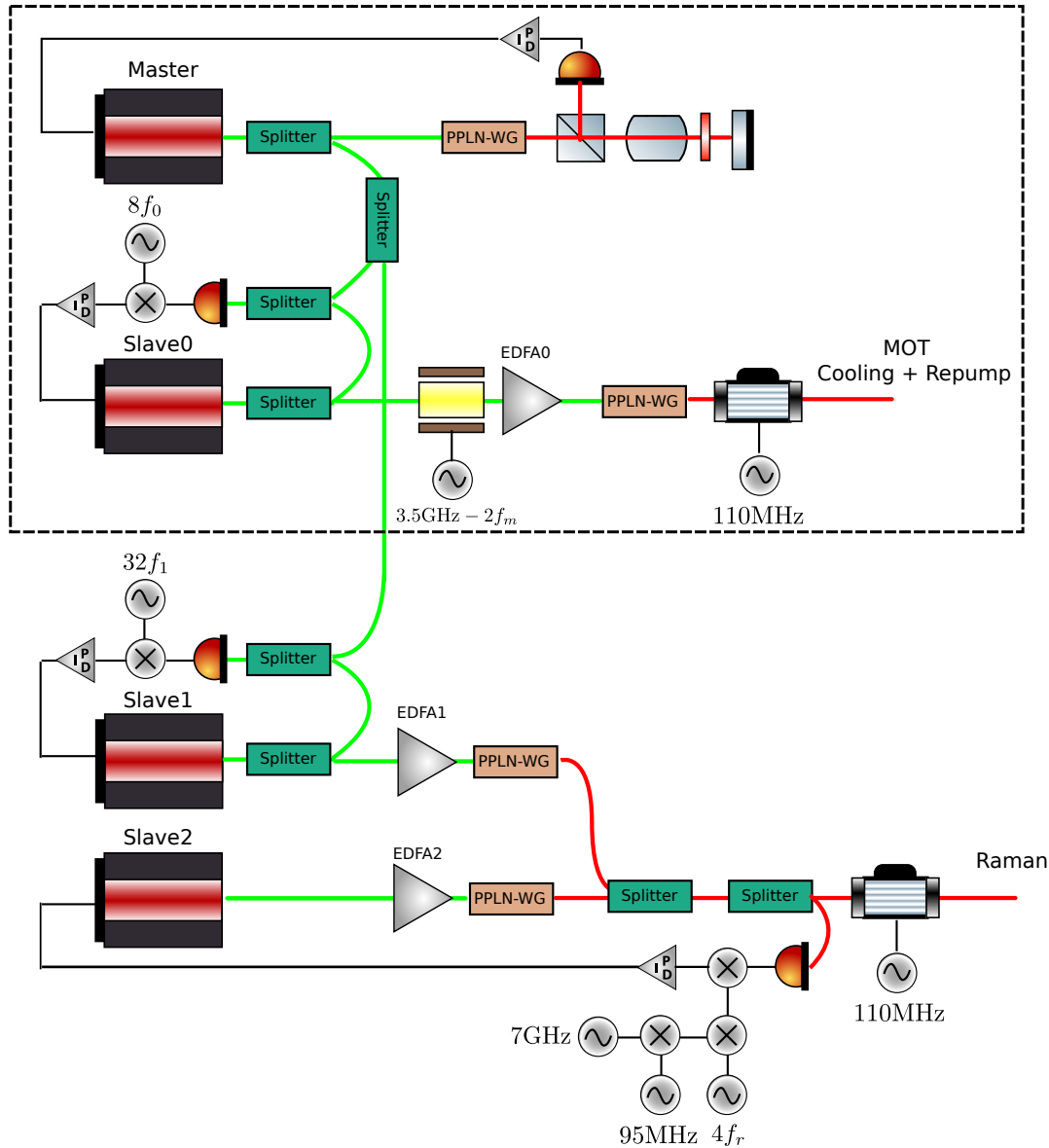
Figure 4.1.: Schematic of the μQuans laser system. Each output laser is derived from a 1560nm ECDL (shown in green) which is amplified using an EDFA and then frequency-doubled to 780nm using a PPLN crystal. A master laser is locked to the 3,4 crossover in ^{85}Rb and the output lasers are offset-locked to their corresponding frequencies. The dashed region indicates the components used for generating light for the MOTs, which was the only function of this laser for this experiment.
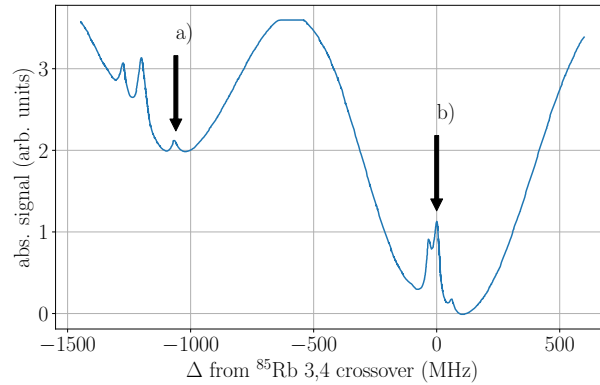
Figure 4.2.: Saturated absorption spectroscopy using the Rubidium vapour cell in the μQuans laser. The absorption features indicated are a): the $F = 2 \rightarrow F' = 3$ transition in ^{87}Rb and b): the crossover resonance between the $F = 3 \rightarrow F' = 3$ and $F = 3 \rightarrow F' = 4$ transitions in ^{85}Rb which is used to lock the frequency of the master laser.

to temperature changes, and under sufficiently weak laser power have linewidths close to the natural linewidth of Rubidium ($\Gamma \sim 2\pi \times 6$MHz). Figure A.2 shows the saturated absorption spectrum using the μQuans master laser. This is obtained by fine adjustment of the temperature of the master External-Cavity Diode Laser (ECDL). The laser is set to lock to the crossover resonance between the $F = 3 \rightarrow F' = 3$ and $F = 3 \rightarrow F' = 4$ transitions in ^{85}Rb (indicated as b)), which is the strongest feature in the spectrum as well as being relatively close the the cooling transition in ^{87}Rb (indicated as a)). Some form of feed-back onto the master laser is required to keep its frequency fixed. The simplest way to achieve this is to use a signal that is linearly proportional to the deviation in frequency from the set-point, if one exists. The frequency of the laser is modulated by weakly modulating the current to the master ECDL. **a**dd more detail about the error signal lineshape The error signal shown in Figure **??** is obtained by demodulating the absorption signal using a lock-in amplifier. In fact, this current modulation is always present on the master laser and the saturated absorption spectrum shown previously has been processed to average out the effects from this fast frequency modulation. In addition to proportional feed-back
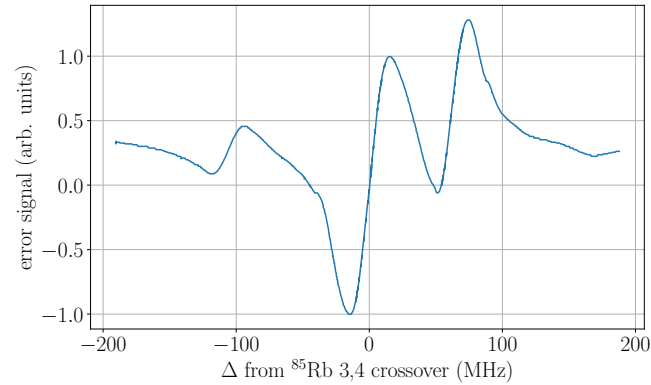
Figure 4.3.: Error signal obtained by modulating the laser current. Close to the lock point, the signal is approximately linear. This signal is used in a feed-back loop to correct for frequency changes of the master laser.

from the error signal, the servo that controls the master frequency also contains an integrator to compensate for long-term drifts. Typically, these arise from external temperature changes and if unaccounted for, they could cause the laser to unlock. In the conditions of our laboratory, where the temperature is externally controlled, this has never occurred.

4.2.2. Generating MOT light

4.2.3. Raman light

4.2.4. Real-time Frequency Control

4.3. The M-Squared Laser System

To-Do:

- Schematic

- Raman PLL phase-noise

- Laser Control

- DCS module

4.3.1. Laser Specifications

4.3.2. The DCS Control Module

4.3.3. Frequency Control of the Raman Lasers

4.3.4. Controlling the Phase Difference

Chapter 5.

Cooling and Trapping in a MOT

5.1. Chapter Outline

5.2. The Navigator Vacuum Chamber

5.2.1. The 2D MOT system

5.2.2. The 3D MOT system

5.2.3. CCD Imaging

5.3. Generating MOT light

5.3.1. Muquans Laser Control

Frequency Control

Real-Time Communication

5.4. Controlling the MOTs

5.4.1. Optical Fibre Network

Chapter 6.

Preparing Atoms for Interferometry

This chapter presents the work that went towards the initial stages of the experimental sequence, where the main objective is to prepare a sufficiently cold ensemble of ^{87}Rb in the same quantum state.

6.1. Chapter Outline

To-Do:

- Discuss loading atoms in 3D MOT from 2D

- Characterisation of the moving frame optical molasses

- Various schemes for preparing atoms into $|1, 0\rangle$. *m*ention velocity selection here or in next chapter?

6.2. Cooling in Optical Molasses

6.2.1. Real-time Frequency Control

6.2.2. Optimising the Temperature

6.3. State Preparation

6.3.1. Schemes for Preparation

6.3.2. Optical Pumping Scheme

6.3.3. Including Microwave Transitions

Wind-Freak Synthesiser

Chapter 7.

Acceleration-Sensitive Interference

This chapter describes the work towards realising an atom interferometer and subsequently measuring accelerations.

7.1. Chapter Outline

To-Do:

- Raman spectrum, identifying each transition

- Characterisation of velocity-selective pulse and each interferometer pulse using Rabi oscillations.

- Making a three-pulse atom interferometer

- Improving acceleration sensitivity and correlating vibrations using MEMS

7.2. Raman Optical System

When designing an optical system for the light used in an atom interferometer, it is worth paying attention to both the spatial extent and beam waist of the collimated beam. These requirements are particularly important in this experiment, where acceleration due to gravity is perpendicular to the Raman beam axis and causes significant transverse motion of the atoms. Firstly, the optical system must be designed to make sure that the atoms are illuminated by each interferometer pulse. In addition to this, a more subtle requirement on the fringe contrast constrains the beam waist size. The gradient of intensity across the atom cloud must be small so that each atom is driven by (approximately) the same Rabi frequency. Otherwise, this variation in the Rabi frequency will dephase the atoms, which reduces the interferometer fringe contrast.

A further constraint on the optical system comes from the effect of thickness variation of optical elements. If the optical path length of the light as it passes through an element is not uniform, this will lead to wavefront aberrations. A spatially-varying phase leads to a bias in the interferometer phase since it does not depend on acceleration. Moreover, since this phase is not the same for each atom, it is another source of dephasing. Considering the effects of wavefront aberrations was a large motivating factor for designing an optical system for use inside the vacuum chamber. Specifically, the distortions of a laser wavefront through optical viewports would drastically reduce the fringe contrast under transverse motion of the atoms during the interferometer. The process used to bond an optical viewport to a flange stresses the glass and distorts its thickness, producing wavefront aberrations that factor into the phase uncertainty of an atom interferometer [**Schkolnik2015**]. Add requirements on other optics

7.2.1. Fringe Contrast Dependence

The effects of a gradient of intensity on the fringe contrast can be shown by considering an ensemble of atoms that are spatially distributed by a Gaussian distribution. Neglecting the effect of the ensemble's velocity distribution on the Raman detuning and for fixed pulse times, the pulse area $\Omega\tau$ varies only as a function of the radial displacement from the optic axis. The total fringe contrast can be determined by a convolution of the contrast for a single atom with the atomic density

$$C = \int \frac{1}{\sqrt{2\pi}\sigma_c} e^{-r^2/(2\sigma_c^2)} f_{\pi/2-\pi-\pi/2}\left(\Omega(r-r_1), \Omega(r-r_2), \Omega(r-r_3)\right) \, \mathrm{d}r \qquad (7.1)$$

where σ_c is the radial width of the atom cloud, $f_{\pi/2-\pi-\pi/2}$ is the fringe contrast as previously described in equation (**??**) and r_i is the position of the ensemble's centre-of-mass at the i-th pulse. If the atom cloud is initially at the centre of the laser and falling under gravity, then these coordinates are $\left(0, -\frac{1}{2}gT^2, -2gT^2\right)$ respectively. Under the assumption that the two lasers which drive the Raman transition have the same waist size, the Rabi frequency, which is determined by the product of the electric fields (see equation (**??**)), can be described by

$$\Omega(r) = \Omega_0 e^{-2r^2/w^2} \qquad (7.2)$$

where Ω_0 is the Rabi frequency along the optic axis and w is the waist size – the distance at which the electric field falls to $1/e$ of its peak value. The fringe contrast as a function as beam waist for an atom cloud of width a width $\sigma_c = 5\,\mathrm{mm}$ and a time between interferometer pulses of $T = 25\,\mathrm{ms}$ is plotted in Figure 7.1. For small beam waists, the intensity gradient across the cloud significantly reduces the fringe contrast. In fact, a beam waist much greater than the width of the cloud is necessary to achieve a large contrast between the two interferometer states. Relaxing the assumptions

made on the ensemble's velocity distribution to include its influence on the detuning and spatial distribution of the atoms during the interferometer would strengthen this argument.
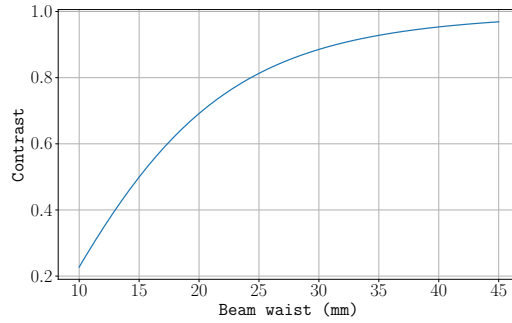

Figure 7.1.: Simulated fringe contrast as a function of waist size w for an atom cloud falling under gravity. This model assumes a Gaussian distributed atomic density with a width $\sigma_c = 5\,\text{mm}$ and a time between interferometer pulses of $T = 25\,\text{ms}$. For smaller beam waists the subsequent interferometer pulses have a larger intensity gradient across the atom ensemble, which increases the dephasing of the two states and reduces the interferometer fringe contrast.

So far, it has been shown that a large beam waist is necessary to achieve a high fringe contrast when allowing for transverse motion of the atoms across the laser wavefront. Otherwise, if the fringe contrast was poor, this would limit the sensitivity of the interferometer to accelerations rather than other effects which are less rectifiable. Another optical effect which influences the sensitivity is distortions of the laser wavefront. In an ideal case, the superposition of the spherical wavefronts of the two lasers results in a planar wavefront for the effective field which drives the Raman transition. However, propagation through rough optical elements distort these wavefronts and introduce a spatially varying component of the Raman phase that is independent of acceleration. If the atom cloud's trajectory is parallel with the Raman axis, then this additional phase is the same at each laser pulse and is therefore cancelled out. Of course, this does not occur when the cloud moves transverse to the Raman axis where this random phase has the effect of reducing the fringe contrast. Starting with the
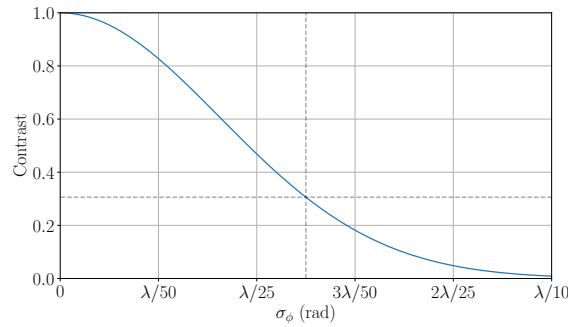
Figure 7.2.: Expected contrast as a function of random phase contributions. This assumes that the phase imprinted on an atom during each interferometer pulse has an additional random component that is Gaussian distributed around 0 with a standard deviation of σ_ϕ. This random phase is also uncorrelated between each pulse so that the total can be obtained using Gaussian propagation of error. The dashed lines indicate the contrast for phase noise expected from conventional optics, which are usually engineered to a surface flatness of $\lambda/20$.

assumption that this phase is Gaussian distributed around 0, with a standard deviation of σ_ϕ, if this is uncorrelated at each interferometer pulse, then the interferometer phase $\Delta\Phi$ will be distributed with a standard deviation of $\sigma_\Phi = \sqrt{6}\sigma_\phi$. Denoting this random phase as $\delta\phi$, the fringe contrast is then given by

$$\mathcal{C}(\delta\phi) = \cos\left(2\delta\phi\right) \tag{7.3}$$

Following from this, if $\delta\phi$ is uncorrelated between each atom, the expected value of the contrast over the ensemble is given by

$$\langle\mathcal{C}\rangle = \frac{1}{\sqrt{2\pi}\sigma_\Phi} \int \mathcal{C}(\delta\phi)\, e^{-\delta\phi^2/2\sigma_\Phi^2}\, \mathrm{d}\delta\phi \tag{7.4}$$

$$= e^{-2\sigma_\Phi^2} \tag{7.5}$$

The value of this expected contrast is plotted in Figure 7.2 and shows a strong dependence on σ_ϕ. Add more justification here. Cite Achim Peter's paper

7.2.2. Raman Beam Collimator

The optical system used to produce the beams for driving Raman transitions, which will conventionally be referred to as the Raman optics, was designed to reduce the previously mentioned effects which result in poorer interferometric fringe visibility and sensitivity to accelerations. Principally, the entire optical system was mounted inside the optical chamber so that the Raman light does not pass through any optical viewports before interacting with the atoms. Typically, the stress placed on the glass during the bonding process will distort the flatness more than is acceptable for achieving a high contrast. For example the viewports used for the MOT optics have a specified flatness of $\lambda/4$, so mounting the entire optical system inside the chamber was the simplest way to avoid a large distortion.

Figure 7.3a presents a diagram of the components used to send Raman light into the chamber and produce a collimated beam in the centre of the chamber. The light is coupled into the chamber using a UHV compatible Polarisation-Maintaining (PM) fibre, manufactured by Diamond photonics. This is a kapton-coated PM-780 HP fibre that is bonded on one end to a DN16 flange using an epoxy resin. The external side of this flange has an FC/APC connector for coupling light from another fibre. Inside the chamber, the ferrule is connected to an FC/APC fibre plate. This is clamped between a piece which bolts onto the inside of a DN63 flange and another stainless steel plate which bolts onto the rest of the optics assembly. Fine adjustment of the position of the fibre along the optic axis is achieved using shim plates with a thickness ranging from 200–300 µm. The fibre plate is free to rotate so that the orientation of the fibre with respect to a Quarter-wave Plate (QWP) at the output of the collimator. This QWP is manufactured by Light Machinery, and is described further is Section 7.2.3. When the fibre is correctly orientated (e.g. when the slow axis of the fibre is at 45deg to the

slow axis of the waveplate), the two Raman light fields are orthogonally circularly polarised.

The original design for the optical system consisted of a triplet lens, as a system of three lenses is capable of correcting for the five types of Seidel aberrations that distort rays of monochromatic light. This was designed and manufactured by IC Optical Systems. Another specification for this lens system was that it had to produce a collimated beam with a waist size of around 35 mm so that the sensitivity of the interferometer was not limited by the effects of intensity gradients across the atoms. Unfortunately, the triplet was designed with an incorrect Numerical Aperture (NA). With a focal length of 123.4 mm and a diameter of 50 mm, the triplet lens has a NA of 0.194. However, the nominal NA for PM780-HP fibre used in the UHV compatible PM fibre is 0.12. Consequently, the light from this fibre did not fill the NA of the triplet lens and produced a beam with a waist of 13mm. Plot to illustrate this. To address this issue, a pair of aspheric lenses was included to increase the divergence angle of light from the fibre. These are manufactured by Thorlabs and have a focal length of 4.51 mm (352230-B) and 15.29 mm (352260-B), respectively, to give a magnification of 3.39.

Alignment and Collimation

As one of the main motivations for mounting the Raman optics inside the vaccuum chamber was to reduce the effects of wavefront distortions, it is worth highlighting how inaccurate alignment of the optics can lead to aberrations. As discussed before (see Section 7.2.1), distortions of the wavefront leads to a dephasing and loss of interferometer fringe visibility. Here, the same figures of merit as before are used to consider what misalignment is acceptable to ensure that the phase of the Raman wavefront deviates by less than $\lambda/100$ after a transverse distance of 12.5 mm.
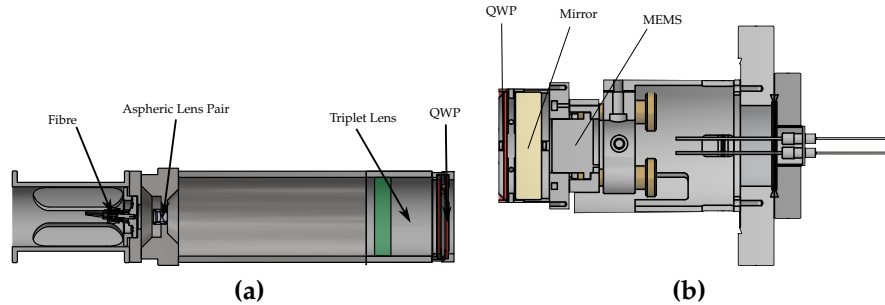
Figure 7.3.: Diagrams of the componets used in the Raman optical assemblies. (a) shows the collimator setup. Light is coupled into the chamber using a UHV fibre feedthrough. A pair of aspheric lenses is used to increase the divergence angle of the fibre output, before the light is collimated by a triplet lens. Finally, a quarter-wave plate is aligned so that it circularly polarises the collimated light fields. (b) illustrates the other half of the setup, which is used to retro-reflect the light. A second quarter-wave plate is used so that the reflected beams have the same handedness to their respected incoming ones. A MEMS accelerometer is mounted on the back of the mirror to measure vibrations. These components are all mounted on a piezo-controlled mirror mount whose tilt can be controlled from outside the vacuum chamber.

Taking the fibre as a point source, misalignment can occur if it is displaced from the front focal point of the optical system longitudinally along or transversely to the optic axis. If it is transversely displaced, this manifests as an angular displacement of the collimated light after the triplet lens. A large angular displacement is undesirable due to the fact that since one of the Raman light fields propagates further, the two wavefronts that drive acceleration-sensitive Raman transitions are not parallel. Figure 7.4a shows a simulation of the wavefront distortion as a result of this transverse misalignment. This is obtained by simulating the propagation of rays corresponding to each Raman light field through the optical system. The wavefront is estimated using the slope of each ray at a distance of 43 mm from the output of the triplet lens, which corresponds to the position of the centre of the vacuum chamber. The mirror is mounted at the same distance from the centre, so the second beam propagates 129 mm. Close to the optic axis, this distortion is approximately linear (i.e. a tilt) and it can be seen that
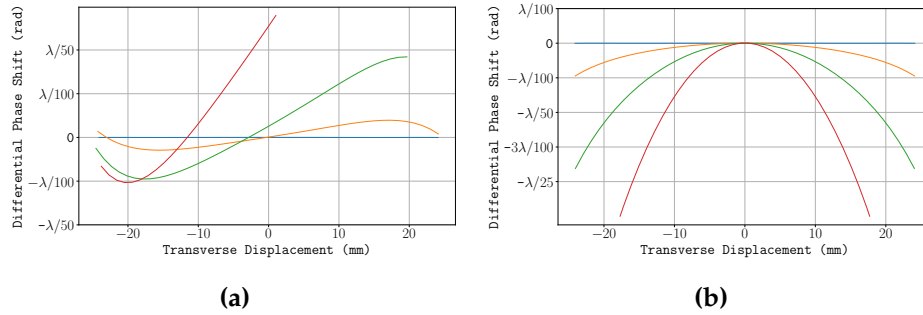
Figure 7.4.: Simulated wavefront distortion for longitudinal and transverse fibre misalignment. Rays from a point source with a divergence angle corresponding to a NA of 0.12 are propagated through the Raman optical system. Rays corresponding to the reflected beam are propagated further with the assumption that the mirror is perpendicular to the optic axis. The first set of rays propagates 43 mm and the second propagates 129 mm. The wavefront for each beam is calculated by taking the slope of each ray and subtracting from the slope of the central ray. The wavefront of the effective field that drives the Raman transition is the difference of these two wavefronts. (a) shows the distortion of the wavefront for a transverse misalignment of the fibre for a displacement of 0 mm (blue), 0.5 mm (orange) 1 mm (green) and 1.5 mm (red) from the front focal point. (b) shows the wavefront for longitudinal displacements of 0 mm (blue), 0.3 mm (orange) 0.6 mm (green) and 1 mm (red).

a displacement of the fibre from the optic axis of <1 mm is sufficient to achieve the desired wavefront flatness.

Aside from a transverse displacement, it is possible that the fibre could be misaligned along the optic axis. In which case, the output beam will not be collimated. Consequently, the counter-propagating reflected rays will not be antiparallel to incoming ones. The effect of this longitudinal displacement on the Raman wavefront is shown in Figure 7.4b. Further from the optic axis the deviation in the phase of the light is greater, giving a quadratic distortion which is characteristic of a defocus. Comparing the wavefront distortion in this case, a requirement on the longitudinal misalignment of < 0.6 mm is needed for the previously specified flatness.

Measuring the Beam Width and Divergence

Most of the characterisation of the beam was taken outside of the vacuum chamber, prior to installation, due to extra difficulties of measuring its properties *in situ*. To measure the beam waist as well as its divergence, the beam was used to illuminate a piece of paper aligned perpendicular to the optic axis. This was then imaged using a CCD camera with an objective lens so the entire spatial extent of the beam could be imaged. The camera was calibrated to give an effective pixel size of 5.1 pix/mm. Both the camera and paper were mounted on a translation stage, so that they could be moved along the direction of propagation. This

7.2.3. Retro-reflection Assembly

The mirror, also manufactured by Light Machinery, that is used to retro-reflect the incoming beams is mounted on the opposite side of the chamber. In order to drive Raman transitions (see Section 7.3 for further detail) with counter-propagating light fields, a second QWP, made to the same specifications as the one in front of the collimation optics, is mounted in front of the mirror. If the forward-propagating fields are circularly polarised, the reflected ones will be polarised with the same handedness regardless of the orientation of this second QWP.

During the manufacturing process, the waveplates and mirror were polished to reduce irregularities in the thickness of each QWP and the surface of the mirror. Figure 7.5 shows the variation in the thickness of the waveplate in front of the triplet lens, measured by Light Machinery using a white light interferometer. This has a standard deviation of 4.62 nm and corresponds a standard deviation of the optical path length of $8.6 \times 10^{-3} \lambda$.
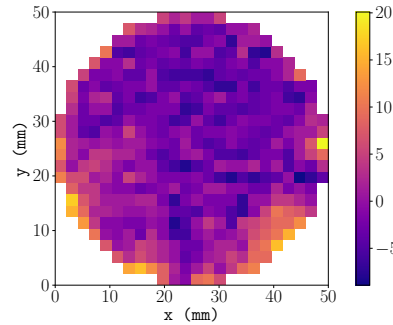
Figure 7.5.: Thickness of the first **QWP!**, measured by a white light interferometer. The value is given in nm as a difference from the mean thickness. The standard deviation of this thickness is 4.62 nm and a peak-to-valley (PV) of **n**eed number here. Equivalent surface data for the other **QWP!** and mirror were not provided by Light Machinery, but had a PV thickness variation of 19 nm and 9 nm respectively.

The QWP and mirror are fixed onto the front plate of a UHV compatible MDI-HS mirror mount, manufactured by Radiant dye. The horizontal and vertical tilt of the mirror can be adjusted using two thumbscrew actuators which cause the front plate to pivot around a ball bearing. This mount is designed for applications which require high stability, but of course the alignment will still drift over time. To avoid the need to periodically open the chamber to realign the mirror, a piezo-electric stack is placed between each actuator and the front plate so that the tilt of the mirror can be adjusted externally. Each piezo-stack is connected to a high-voltage feedthrough, so that their length (and hence mirror tilt) can be finely adjusted by controlling the voltage applied across them. A control voltage ranging between 0–10 V is amplified by a controller to give an applied voltage across the piezo stack that ranges between -10–150 V, corresponding to a travel range of 23 μm.

To understand the effect of misalignment, it is instructive to consider its effect on the effective wavevector $\mathbf{k}_{\text{eff}}$. As illustrated in Figure **??**, if the mirror is misaligned from the incoming beam's wavevector by an angle *theta*, the two counter-propagating fields that drive Raman transitions have wavevectors $k_1 (1,0)$ and $k_2 (\cos(\theta), \sin(\theta))$. $\mathbf{k}_{\text{eff}} = \mathbf{k}_1 - \mathbf{k}_2 \cos(2\theta_i)$. Fortunately, for small angular displacements, i.e. < 1 mrad,

this does not greatly reduce the sensitivity to accelerations. In short, this means that $\mathbf{k}_{\text{eff}}$ will have a spatially varying direction. Since an atom interacting via a Raman transition picks up a phase $\phi = \mathbf{k}_{\text{eff}}.\mathbf{x}$, atoms travelling along different trajectories will accumulate different phases due to the spatial variation of $\mathbf{k}_{\text{eff}}$. Across the atom ensemble, this leads to a dephasing and consequently, a loss of interferometer fringe visibility [4]

In-Situ Alignment and Optimisation

After mounting the Raman optical system inside the chamber, the mirror had to be aligned to retro-reflect the light. When the mirror is close to perpendicular to the light's wavevector, some of the power in the reflected beam couples back into the fibre. In principle, this power is maximised when the mirror is exactly perpendicular so maximising this power is a useful technique to align the mirror. A 99:1 fibre splitter was used to couple light into the chamber, which provided a means to measure the back-reflected power without needing any free-space optics. This was set up so that 99% of the incoming light entered the chamber, with the other 1% coupled into the corresponding output port. Due to the fact that a beam-splitter acts reversibly, 1% of the back-reflected light which couples into vacuum fibre exits the fibre-splitter on the other input port. Therefore, the power at this output was used to indirectly measure the alignment of the mirror.

Since the travel range of the piezo stacks does not cover the full motional range of the mirror mount, the mirror initially had to be manually aligned using the thumb-screw actuators. Once installed, the lack of direct access to optical system meant that conventional methods to coarsely align the mirror, such as observing the location of the reflected beam's focus, were not feasible. Rather than carry out the somewhat tedious job of systematically adjusting each thumbscrew until the mirror was aligned,

an automatic routine was devised to do this. This was carried out using a pair of bipolar stepper motors that each rotated a ball driver inserted into the head of each thumbscrew. The revolution of these motors was controlled using an arduino micro-controller, which communicated to the computer using a serial interface. The motors rotated by 0.9deg/step, which corresponds to a tilt of the mirror by 18.1 µrad. This is smaller than the 0.67 mrad angular displacement that the piezo stack could provide, but the slow execution speed of the motor control meant that it was more practical to use a combination of the motors and piezos to systematically scan through the tilt of the mirror mount. **huge find out how big spot size was** .

Using this method, the mirror mount was aligned so that the the maximum of the back-reflected power was reachable with the piezo stacks. Of course, it was forseeable that the mirror would need to be periodically realigned, which would require another systematic iteration through the voltages applied to each piezo stack. Given that this search was quite time consuming, it was not a practical way to maintain alignment. To improve upon this, an optimisation method using the Nelder-Mead simplex algorithm [3] was implemented. This method is suitable for optimising multidimensional functions and has been used to demonstrate the automatic alignment of a fibre with up to 6 degrees of freedom [5]. In general terms, this algorithm aims to optimise the value of an objective function (in this instance, the optical power measured as a voltage by a photodiode) by sampling the function at various locations. For n parameters, a set of $n - 1$ points distributed randomly across the parameter space are chosen as the initial simplex. These are sorted in decreasing order of the value of the obejctive function and the algorithm proceeds by performing geometric transformations on this simplex, by sequentially reflecting, expanding and contracting this simplex. Each step starts with a reflection about the line between the two greatest values. The coordinates of the simplex are updated if the function has a greater value at the location given by one of these transformations, until the algorithm converges on a maximum value. As

with many optimisation algorithms, the Nelder-Mead method has the potential to converge on a local optimum, but this is allieviated by expanding the simplex to look for more optimal values. The termination of the algorithm was decided by using the standard deviation of the last 5 values. Empirically, it was found that terminating when the standard deviation was less than $10\,\mu V$ resulted in stable performance of the algorithm, even when the signal-to-noise ratio of the measured voltage was poor. An example of this algorithm aligning the mirror mount is presented in Figure 7.6. To verify that the converged value was optimal, a systematic scan of the piezo stack control voltages in the region around this value was also carried out. In this case, the algorithm converged on a local maximum, but one that greatly enhanced the coupling efficiency of the reflected light back into the fibre. The difference in the piezo control voltages from their optimal values corresponds to a tilt of the mirror mount along the horizontal and vertical axis of less than $13\,\mu rad$.

7.2.4. The MEMS Accelerometer

7.3. Driving Raman Transitions

As the forward-propagating fields have opposite handedness, the counter-propagating fields have the same handedness as the field
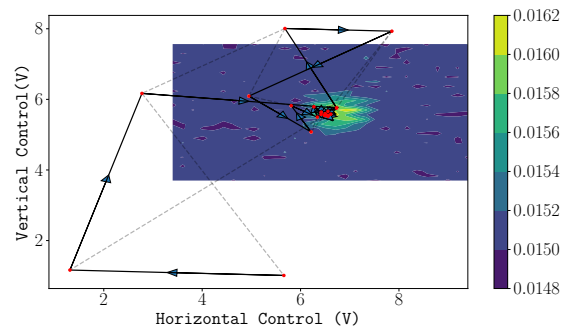
Figure 7.6.: Automatic mirror alignment using the Nelder-Mead simplex algorithm. This procedure starts by randomly selecting three pairs of control voltages for the horizontal and vertical piezo stacks. At each co-ordinate, the back-reflected power is measured. The algorithm proceeds by geometrically transforming the simplex using reflections, expansions and contractions, and updating the simplex using this new co-ordinate if the power measured is greater than the current lowest value. The algorithm uses the standard deviation of the last 5 values as a check for convergence. In this case, it terminates once the standard deviation is smaller than 10 μV. The shaded lines indicate the simplex bounded by the three co-ordinates at each iteration, whose area reduces as the algorithm converges on the optimum value. A scan of the piezo control voltages close to the optimum is also plotted. The irregular shape of the measured power is a result of a hysteresis effect when the horizontal control voltage was changed from its maximum value to the minimum. Even with a low signal-to-noise ratio, the algorithm converged on a value close to the optimum. This resulted in a misalignment of less than 13 μrad along both axes.

7.3.1. Frequency and Phase Control

7.4. Atom Detection

7.4.1. Optical System

7.4.2. Measuring the Interferometer Phase

7.5. Individual Pulse Characterisation

7.5.1. Velocity-Selective Pulse

7.5.2. Interferometer Pulses

7.6. Three-Pulse Atom Interference

7.7. Measuring Accelerations

7.7.1. Vibration Sensitivity

Chapter 8.

Outlook

This final chapter describes some of the next steps and further work

8.1. Combining with classical accelerometers

- Discuss schemes for combining multiple sensors - Kalman filtering

- Extend this to inertial navigation

- Steps towards overcoming sensitivity-bandwidth trade-off.

8.2. Extending to senstivity along three axes

- New chamber design

- Improvements to MSquared laser

- Required knowledge of gravitational axis for accurate navigation

Bibliography

[1]   Aviv Keshet and Wolfgang Ketterle. "A Distributed GUI-based Computer Control System for Atomic Physics Experiments". In: (2012). DOI: 10.1063/1.4773536. arXiv: 1208.2607.

[2]   *μQuans Laser System Specifications*.

[3]   J. A. Nelder and R. Mead. "A Simplex Method for Function Minimization". In: *The Computer Journal* 7.4 (1965), pp. 308–313. ISSN: 0010-4620. DOI: 10.1093/comjnl/7.4.308.

[4]   G Tackmann et al. "Self-alignment of a compact large-area atomic Sagnac interferometer". In: *New Journal of Physics* 14.1 (2012), p. 015002. ISSN: 1367-2630. DOI: 10.1088/1367-2630/14/1/015002.

[5]   R. Zhang and F.G. Shi. "A Novel Algorithm for Fiber-Optic Alignment Automation". In: *IEEE Transactions on Advanced Packaging* 27.1 (2004), pp. 173–178. ISSN: 1521-3323. DOI: 10.1109/TADVP.2004.825434.

Acronyms

CCM Centre for Cold Matter

^{87}Rb Rubidium-87

^{85}Rb Rubidium-85

MOT Magneto-optical Trap

AOM Acousto-optic Modulator

EOM Electro-optic Modulator

PM Polarisation-Maintaining

QWP Quarter-wave Plate

HWP Half-wave Plate

MFD Mode Field Diameter

NA Numerical Aperture

PPLN Periodically Poled Lithium Niobate

PLL Phase-Locked Loop

FPGA Field-Programmable Gate Array

EDFA Erbium-Doped Fibre Amplifier

ECDL External-Cavity Diode Laser

TTL Transistor-transistor Logic Circuit

NI National Instruments

DAQ Data Acquisition

VCO Voltage-Controlled Oscillator

ADC Analogue-to-Digital Converter

DAC Digital-to-Analogue Converter

HAL Hardware Abstraction Layer

SPI Serial Programming Interface

DDS Direct Digital Synthesiser

PBS Polarising beam-splitter

DRO Dielectric Resonator Oscillator

Appendix A.

Laser Systems

This chapter provides a description of the hardware that makes up the experiment. Over the course of the project, the complexity of the experiment necessarily increased. The setup is presented in a bottom-up approach, starting from the most fundamental components, to provide a clear overview of the system.

To-Do:

- Figures describing each of the lasers

- Describe 3D and 2D MOT setups

- Imaging systems

- Microwave synthesisers

- Raman Assembly

- MOT light distribution

A.1. Chapter Overview

The first two sections describe the two commercial laser systems used in this experiment. The μQuans laser system which generates the light used for cooling and repump in the 2D and 3D MOTs, referred to as the MOT light. The design and operation of this laser is given in Section A.2. A secondary laser system, built by MSquared, is used to generate light to drive Raman transitions between two hyperfine ground states in

[87]Rb[1], otherwise referred to as Raman light. This is described in Section A.3. This is followed by a description of the vacuum chamber in Section **??** which contains both the 2D MOT (Section **??**) and the 3D MOT (Section **??**).

A.2. The μQuans Laser System

To-Do:

- Laser Schematic

- Plots of lock signals

- DDS Serial communication

- Power output, stability

- Ref for error signal generation by current modulation

- Move some of this to appendix

All the MOT light in this experiment was generated by the μQuans laser [2]. μQuans is a French laser company that is a spin-off from the Institut d'Optique and Observatoire de Paris. Consequently, their technology has been developed over a long history of performing experiments into atom interferometry using Rubidium. A schematic of this laser system is shown in Figure A.1. The μQuans laser is comprised of four 1560nm **ecdls!**s which are frequency-doubled to produce light at wavelengths close to 780nm. The telecommunications industry, which relies heavily on light in the 1530–1565nm wavelength band for optical communications, has motivated a rapid development in low-noise, robust lasers. In particular, this has enabled a design which does not require free-space optics and is much more resilient to effects such as temperature changes and vibrations, when compared to more conventional 780nm laser systems. The μQuans laser contains one master laser[2], which is locked to the $F = 3 \rightarrow F' = 3, 4$ crossover point in [85]Rb, and serves as an absolute frequency reference. The other three slave lasers are used for output. The first one is used to provide light for cooling, as well as repump light by modulating the phase of this laser using an EOM. The other two make up a pair of lasers for driving Raman transitions. One laser is frequency-offset locked

---

[1]The μQuans laser also has a pair of lasers designed for driving Raman transitions, but these are not used in this experiment. Section A.3 gives an explanation for this.
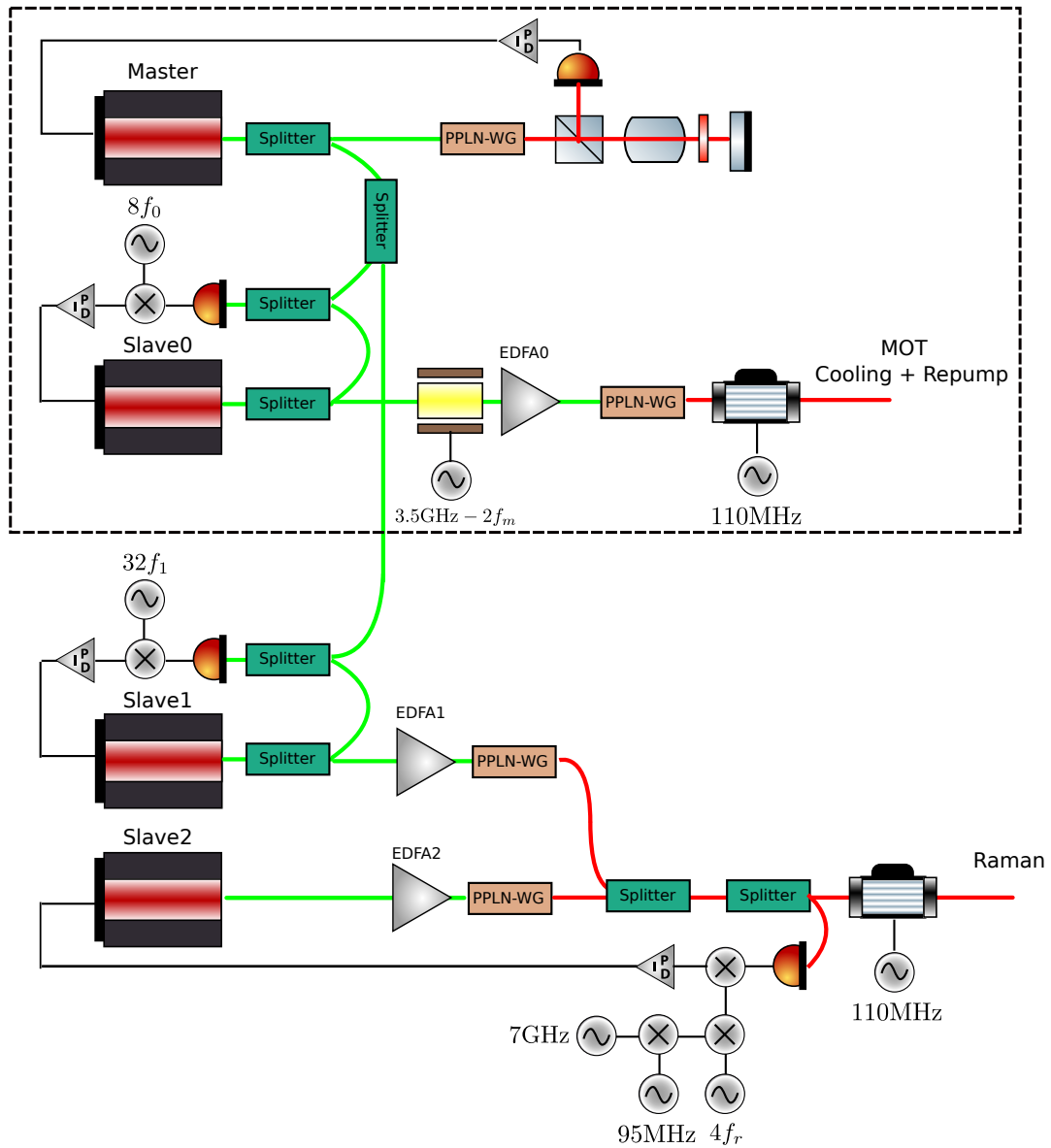
[2]see Section A.2.1 for more details

Figure A.1.: Schematic of the μQuans laser system. Each output laser is derived from a 1560nm
ECDL (shown in green) which is amplified using an EDFA and then frequency-
doubled to 780nm using a PPLN crystal. A master laser is locked to the 3,4
crossover in ^{85}Rb and the output lasers are offset-locked to their corresponding
frequencies. The dashed region indicates the components used for generating
light for the MOTs, which was the only function of this laser for this experiment.

to the master and the other is phase-locked to the first, to ensure that the relative phase
between the two lasers is constant. It should be noted that this Raman laser was not
used in this experiment, so will not be discussed in great detail. Each of these slave
lasers is amplified in an EDFA before being frequency doubled in a PPLN and passed
through an AOM which is used to control the output power during the experiment.
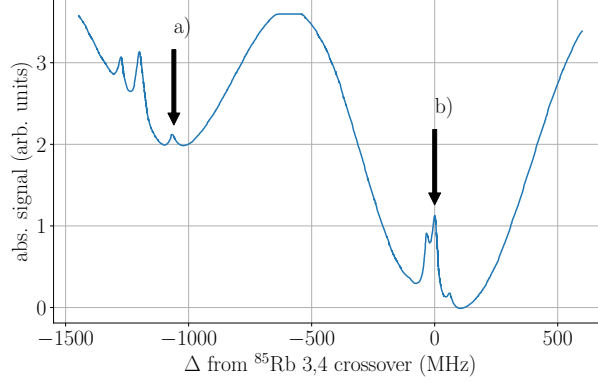
Figure A.2.: Saturated absorption spectroscopy using the Rubidium vapour cell in the μQuans laser. The absorption features indicated are a: the $F = 2 \to F' = 3$ transition in ^{87}Rb and b: the crossover resonance between the $F = 3 \to F' = 3$ and $F = 3 \to F' = 4$ transitions in ^{85}Rb which is used to lock the frequency of the master laser.

A.2.1. Absolute Frequency Reference

The purpose of the master laser is to provide an absolute frequency reference so that the frequency of the output lasers can be controlled by comparing the difference frequency between them and the master. Lasers with linewidths narrower than their natural linewidth can be achieved by using a servo to stabilise their frequency and is essential for any experiment that requires laser light of a precise frequency. The frequency reference for the master is obtained using saturated absorption spectroscopy inside a Rubidium vapour cell. The sub-Doppler features in this spectrum are insensitive to temperature changes, and under sufficiently weak laser power have linewidths close to the natural linewidth of Rubidium ($\Gamma \sim 2\pi \times 6$MHz). Figure A.2 shows the saturated absorption spectrum using the

Muquans master laser. This is obtained by fine adjustment of the temperature of the master ECDL. The laser is set to lock to the crossover resonance between the $F = 3 \to F' = 3$ and $F = 3 \to F' = 4$ transitions in ^{85}Rb (indicated as b), which is the strongest feature in the spectrum as well as being relatively close the the cooling transition in ^{87}Rb (indicated as a). Some form of feed-back onto the master laser is required to keep its frequency fixed. The simplest way to achieve this is to use a signal that is linearly proportional to the deviation in frequency from the set-point, if one exists. The frequency of the laser is modulated by weakly modulating the current to the master ECDL. **a**dd more detail about the error signal lineshape The error signal shown in Figure **??** is obtained by demodulating the absorption signal using a lock-in
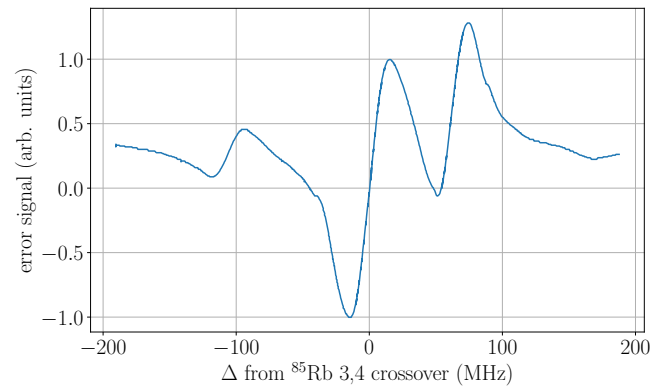
Figure A.3.: Error signal obtained by modulating the laser current. Close to the lock point, the signal is approximately linear. This signal is used in a feed-back loop to correct for frequency changes of the master laser.

amplifier. In fact, this current modulation is always present on the master laser and the saturated absorption spectrum shown previously has been processed to average out the effects from this fast frequency modulation. In addition to proportional feed-back from the error signal, the servo that controls the master frequency also contains an integrator to compensate for long-term drifts. Typically, these arise from external temperature changes and if unaccounted for, they could cause the laser to unlock. In the conditions of our laboratory, where the temperature is externally controlled, this has never occurred.

A.2.2. Generating MOT light

A.2.3. Raman light

A.2.4. Real-time Frequency Control

A.3. The M-Squared Laser System

To-Do:

- Schematic

- Raman PLL phase-noise

- Laser Control

- DCS module

A.3.1. Laser Specifications

A.3.2. The DCS Control Module

A.3.3. Frequency Control of the Raman Lasers

A.3.4. Controlling the Phase Difference